Paper Number 161

# TRANSITORY SEPARATION CONTROL ON A ROBIN FUSELAGE USING PULSED ACTUATION

George T. K. Woo and Ari Glezer
Woodruff School of Mechanical Engineering
Georgia Institute of Technology, Atlanta GA, 30332, USA
E-mail: gtkwoo@gatech.edu & ari.glezer@me.gatech.edu

Thomas M. Crittenden
Virtual AeroSurface Technologies Inc.
Atlanta GA, 30332, USA
tom.crittenden@vastechnologies.com

## ABSTRACT

Separation control of the 3-D flow over the aft body of a scale model of NASA's ROBIN mod7 rotorcraft fuselage is investigated in wind tunnel experiments using successive pulsed actuation effected by arrays of miniature combustion-based actuators. The actuation leads to the formation of momentary jets having a characteristic time scale O[1 ms] that is an order of magnitude shorter than the convective time scale of the flow. These actuators are placed upstream of the transition region between the fuselage and the tail boom, and their interactions with the massively separated cross flow in this domain and, consequently, their effects on the global aerodynamic forces and moments are investigated using an onboard load cell and measurements of the velocity field using high resolution PIV that is acquired phase-locked to the actuation waveform. Symmetric actuation about the model's centerline can significantly mitigate separation, and lead to a reduction in drag and lift, and changes in the pitching moment. Asymmetric actuation, and consequently non-uniform attachment can induce large side forces, roll and yaw that can be exploited for steering and improved flight maneuverability.

## NOMENCLATURE

| | | |
|---|---|---|
| $R$ | = | Fuselage reference length |
| $L$ | = | $2R$, Fuselage overall length |
| $\alpha$ | = | Fuselage angle of attack |
| $T_{conv}$ | = | Convective time scale |
| $U_\infty$ | = | Freestream velocity |
| $Re_L$ | = | Reynolds number based on fuselage length |
| $T_{burst}$ | = | Actuation burst period |
| $T_{pulse}$ | = | Time between actuation pulses |
| $T_{delay}$ | = | Time between actuation bursts |
| $N$ | = | Number of actuation pulses in burst |
| $C_P$ | = | Pressure coefficient |
| $x, y, z$ | = | Streamwise, vertical and cross-stream coordinates |
| $u, v$ | = | Streamwise and vertical velocities |
| $C_L$, $C_S$, $C_D$ | = | Lift, side and drag force coefficients |
| $C_{M,x}$, $C_{M,y}$, $C_{M,z}$ | = | Roll, yaw and pitching moment coefficients |

## I. INTRODUCTION

Heavy-lift rotorcraft and fixed wing cargo aircraft typically experience significant pressure drag during normal flight conditions due to the inherently three-dimensional bluff-body fuselage designs where a massively separated flow region is formed over the rear body which typically has a slanted-surface inclination. The drag adversely affects forward flight speed and fuel economy. The utility of various flow control approaches based on a combination of passive, active and hybrid actuation for the mitigation of flow separation on two-dimensional lifting surfaces has been demonstrated in numerous investigations. Specifically, a number of investigators have used time-harmonic actuation based on synthetic jets for suppression of separation with varying degrees of success (Ahuja and Burrin, 1984, Neuburger and Wygnanski, 1987, Seifert et al., 1996, Honohan et al., 2000, Greenblatt and Wygnanski, 2001, Tuck and Soria, 2004, Glezer et al., 2005, and Sosa et al., 2006). A different approach to separation control that is based on transitory, pulsed actuation which is applied on time scales that are significantly shorter than the characteristic advection time over the separated flow domain was demonstrated to achieve substantial control authority by Brzozowski and Glezer (2006), Woo et al., (2008 and 2009) and Brzozowski et al., (2010). This approach was later extended by Woo et al., (2010 and 2011) to control dynamic stall using staged-pulsed actuation and was effective in suppression of the highly transitory stalled flow to increase the cyclic lift and reduce the undesirable aerodynamic loading induced by the negative damping in the pitching moment.

The primary control challenge for rotorcraft fuselage is that the separation over the fuselage is three-dimensional in nature and the extent of the separation region is massive. Furthermore, because the magnitude and direction of the aerodynamic forces and moments are strongly coupled to the separation, effective control of the separation can achieve significant control of the aerodynamic forces for steering and stabilization. In the recent wind tunnel experiments by Woo et al. (2011), the use of pulsed actuation was implemented on a ROBIN fuselage and a significant drag reduction was demonstrated. The present work builds on the earlier findings to exploit segmented actuation of the separated flow in the transition region between

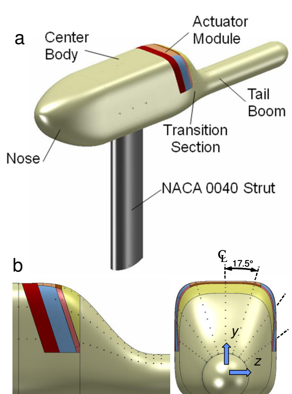


***Figure 1.*** *The wind tunnel assembly showing the ROBIN mod7 fuselage and COMPACT module (a) and the static pressure ports on transition section (b).*

the cabin and tail boom to achieve significant side forces, and yaw and roll moments for steering. §II describes the experimental set-up, including the model design, actuator placement, and diagnostics. §III describes experimental characterization of the baseline flow over the model in the absence of actuation. The quasi-steady dynamics of the flow in response to successive pulsed actuation on the separated flow and drag reduction are described in §IV, and control of aerodynamic steering side forces by transitory flow attachment is discussed in §V.

## II. EXPERIMENTAL SET-UP AND METHODOLOGY

The present experiments use an isolated rotorcraft fuselage based on NASA's ROBIN (ROtor Body INteraction) mod7 generic model (overall length $L = 2R = 914$ mm) as shown in Figure 1. The model's transition segment is instrumented with a six-unit assembly of approximately 2cm$^3$ COMPACT actuators and it is mounted in the wind tunnel upside down with the angle of attack adjustable between +5° and -5°. A six-component force balance is mounted inside the model to measure the time-dependent, aerodynamic forces and moments. The experiments are conducted in an open return wind tunnel having a test section measuring 0.91 x 0.91 m (36 x 36") and with free stream speed up to $U_\infty = 40$ m/s ($Re_L = 570{,}000$ based on the model length, and a convective time scale over the fuselage of $T_{\mathrm{conv}} \approx 23$ ms). Further detailed descriptions of the model are given in Woo et al. (2011). The flow over the transition section is characterized using phase-locked, high-speed particle image velocimetry (PIV) in multiple cross-stream planes. For each view, sets of PIV images are captured at a sequence of predetermined time delays relative to the actuation signal. The centerline of the fuselage is instrumented with 23 static pressure ports on the bottom surface from the nose to the end of the transition section of the model, which has a total of 133 ports in seven rows spaced at 17.5° apart (Figure 1b). Each port is connected to an external high-speed PSI pressure measurement system.

As noted above, two independently-addressable actuator arrays located on the bottom surface at $x_o/R = 1.04$ (note that $x_o$ and $y_o$ are relative to the fuselage nose) provide momentary [O(1 ms)] combustion-based pulsed jets (see Woo et al., 2011). COMPACT (Combustion Powered Actuation) is a novel actuation technology which exploits the chemical energy of gaseous fuel/oxidizer mixture to create a high pressure burst and subsequent high momentum jet of exhaust products. Details of the COMPACT technology are described by Crittenden, et al. (2001 and 2006). In this paper, the non-premixed mixture of air and hydrogen is ignited using miniature sparks driven by a computer-controlled electronic ignition system to produce supersonic pulsed jets at the orifices. The jets issue tangential to the fuselage surface through six equally-spaced (3.2 mm apart) rectangular orifices each measuring 16.7 mm in the spanwise direction 0.2 mm wide. The actuation is characterized by the repetition time between pulses $T_{\mathrm{pulse}}$, the number of pulses within a "burst" $N$, and the delay between successive bursts $T_{\mathrm{delay}}$ (*cf.* Figure 16 in §IV). Performance characteristics of these actuators are described by Woo et al. (2008 and 2009).

## III. THREE-DIMENSIONAL BASELINE SEPARATION

The basic aerodynamic characteristics of the ROBIN model and the extent of the baseline, 3-D separation are

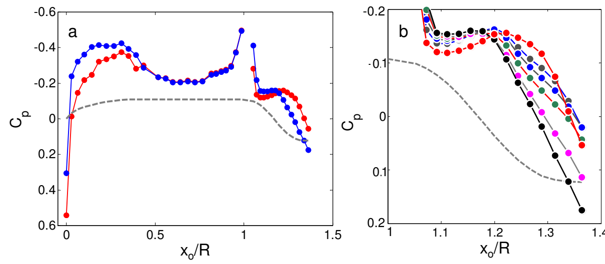


***Figure 2*** *a) Centerline pressure distribution (z = 0) over the bottom surface for the baseline model at pitch angles $\alpha = 0$ (●) and -5°(●), and b) the pressure over the transition region for $\alpha = 0$ (●), -1 (●), -2 (●), -3 (●), -4 (●), and -5°(●) (at $Re_L = 570{,}0000$). The bottom surface is outlined in (—).*

investigated over a range of angles of attack and Reynolds numbers. The centerline pressure distributions on the bottom surface of the model (which is inverted in the tunnel) at the fuselage are shown in Figure 2a for pitch angles $\alpha = 0$ and -5° at $U_\infty = 40$ m/s. These data exhibit a significant suction peak within the domain $0 < x_o/R < 0.5$ as the flow accelerates over the convex curved nose region. At $\alpha = -5°$, this suction peak is higher and more gradual than at $\alpha = 0°$ due to the reduced relative angle between model surface and the free stream. It is noteworthy that the pressure at $x_o/R = 0$ for $\alpha = -5°$ ($C_P = 0.3$) is significantly lower than for $\alpha = 0°$ ($C_P = 0.54$). Perhaps more prominent is a second, much stronger suction peak upstream of the transition section ($0.76 < x_o/R < 1.0$). Over the upstream segment of the transition section ($1.0 < x_o/R < 1.2$), the pressure is higher for $\alpha = 0°$ than $\alpha = -5°$. However, for $x_o/R > 1.2$, the suction at $\alpha = 0°$ is more negative than at $\alpha = -5°$. Centerline pressure distributions over the transition region for $0 < \alpha < -5°$ are shown in Figure 2b and exhibit a faster pressure recovery as the angle of attack increases indicating that the extent of the separation domain diminishes. This pattern is confirmed using time-averaged PIV data in the centerline plane of the model (Figure 3) that are obtained at three angles of attack ($\alpha = 0$, -2.5, and -5°), and three different free stream velocities ($U_\infty = 20$, 30, and 40 m/s) showing the average velocity field (using 400 image pairs). These data show the extent of the separation over the transition surface where the separating shear layer is rather prominent. These images also show some evidence of reversed flow near the surface. It is noteworthy that the size of the separated flow domain decreases with the

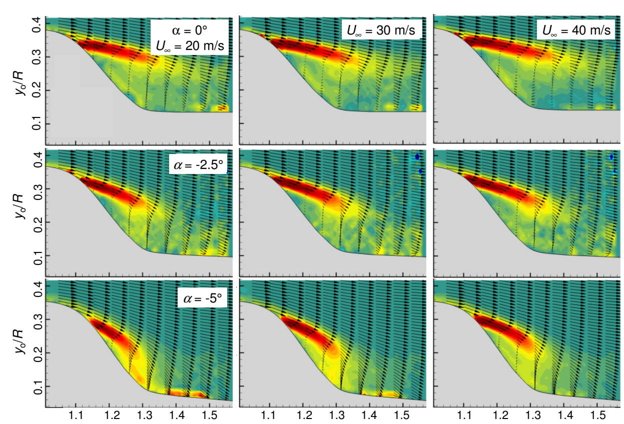


***Figure 3*** *Normalized velocity vectors and vorticity concentrations from PIV measurements of the flow along the centerline of the transition region for variation in angle of attack (rows) and free stream velocity (columns). $\omega L/U_\infty$: -60 60*

increase in the magnitude of (nose-down) angle of attack as a result of the reduced flow turning and reduced blockage from the tail boom. The degree of flow separation appears to be less sensitive to the free stream speed. The 3-D baseline separation is shown using a sample of surface oil visualization in Figure 4 for $\alpha = 0^{\circ}$ and $U_{\infty} = 40$ m/s. This image shows a line of oil build-up along the top of the transition region and down along the sides of the model. The image indicates that the full 3-D separation line is nominally straight along the span of the flat fuselage bottom at approximately $x_o/R = 1.04$, progresses along the sides of the fuselage at an angle of 18°, and ultimately vanishes along the boom. The location of the actuator arrays (§III) is determined from the 3-D separation line.

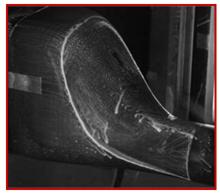

***Figure 4*** *Surface oil visualization shows separation line for $\alpha = 0^{\circ}$ and $U_{\infty} = 40$ m/s.*

The variation of the drag with angle of attack measured directly using the internal load cell that is integrated into the model is shown in Figure 5. These data show that the drag decreases slightly with a minimum around -1° and then increases rapidly ostensibly owing to the increased drag on the front body and on the tail boom (as indicated by the pressure distributions in Figure 2). Therefore, it is expected that separation control over the transition section yields the largest reduction in pressure drag at lower $\alpha$ at which the pressure drag is dominated by the separated flow.

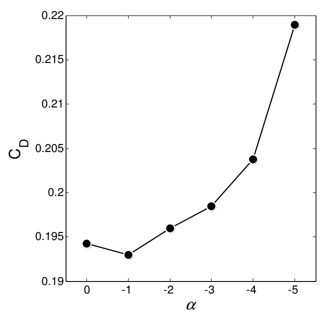


***Figure 5*** *Drag variations with fuselage $\alpha$ at $U_{\infty} = 40$m/s.*

## IV. SEPARATION CONTROL USING REPETITIVE PULSED ACTUATION

The effects of pulsed actuation to control the aggressively 3-D separated flow over the transition section of the model are investigated at $\alpha = 0^{\circ}$ using repetitive pulsed actuation. The first set of results are for the actuation configuration where the two actuator arrays are triggered simultaneously and the repetition rate is set so that $T_{\text{pulse}} = 0.87T_{\text{conv}}$. Figure 6 shows the time-averaged pressure distribution along the model's centerline for the baseline flow and in the presence of actuation (the outline of the bottom surface is also shown for reference). These data demonstrate significant pressure recovery over the model's transition section in the presence of actuation (in the domain $x_o/R > 1.1$, the pressure rapidly increases from $C_p \approx -0.6$ to 0.35), and also indicate that the actuation has minimal effect within the domain

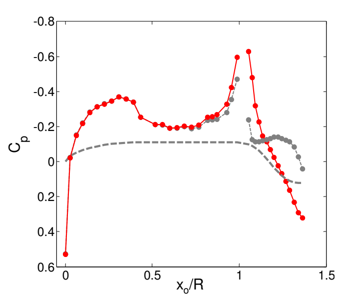


***Figure 6*** *Centerline ($z = 0$) pressure distribution over the bottom surface for $\alpha = 0$ in the absence (●) and presence (●) of actuation at $Re_L = 570{,}000$. The outline of the bottom surface is also shown for reference (—).*

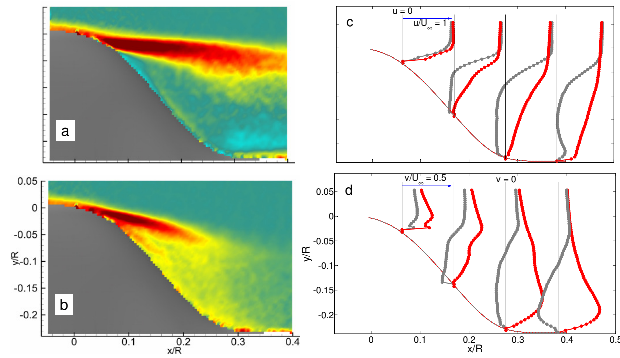


***Figure 7*** *PIV measurements in the centerplane $z = 0$ over transition section in the absence (a) and presence (b) of pulsed actuation showing vorticity concentration contours. Included are the cross-stream profiles of the normalized velocities in the positive x- (c), and negative y- (d) directions for the baseline (●) and actuated (●) flows. $\omega L/U_{\infty}$: -60 60*

$x_o/R < 0.75$. The actuation results in an increase in suction pressure over the surface from $0.75 < x_o/R < 1.4$ along with significant rise in the suction peak upstream of the transition section and a slight migration upstream indicating that the momentum of the flow along the surface increases with actuation. There is no indication of flow separation within the measurement domain in the center plane.

While lift recovery that is associated with controlled reattachment of the stalled flow over 2- and 3-D surfaces can be accompanied by an increase in the (lift-induced) drag, the present actuation is adjusted so that the flow attachment over the transition section (*cf.*, Figure 6) results in a *decrease* in pressure drag. By reducing the asymmetry between the pressure distributions on the nose and transition sections, the total drag on the fuselage decreases by 12% from $C_{D,0} = 0.174$ to $C_D = 0.152$. However, the flow attachment is also accompanied by a significant decrease in lift on the platform to $C_L = -0.182$. The measured aerodynamic effects in connection to the repetitive actuation in Figure 6 can be explained by the differences in the flow field for the baseline and controlled ($T_{\text{pulse}} = 0.87T_{\text{conv}}$) cases as shown in the time-averaged PIV images (using 200 image pairs) taken in the centerline plane $z = 0$ (Figure 7). In Figure 7a, the time-averaged vorticity concentrations show the extent of the separation over the transition surface where the separating shear layer is rather prominent and it extends over $x = 0.4R$ (note that $x$ and $y$ are relative to the actuator orifice location) in the streamwise direction towards the tail boom highlighting the massive baseline separation over the ramp. In the presence of actuation (Figure 7b), it is remarkable that the shear layer is controlled such that its streamwise extent is significantly reduced to only $x = 0.3R$. It is also evident that the shear layer is vectored towards the surface with actuation and that there is an increase in accumulation of the vorticity concentrations close to the curved surface over the transition section.

Included in Figure 7 are the corresponding cross-stream profiles of the two velocities ($u$, $-v$) at different streamwise locations in the transition section. The baseline $x$-component velocity profiles show significant reverse flow and large velocity gradients $du/dy$ across the shear layer while with actuation, the profiles show no reversed flow but significant increase in flow velocity (Figure 7c). There is also evidence that with the smaller velocity gradients $du/dy$, the flow velocity over the ramp is higher. In connection to the reversed flow, there is significant flow up (Figure 7d) along the ramp (i.e. $v \geq 0$), but this is suppressed with the actuation and flow is vectored towards the model (i.e. $v \leq 0$). The cross-stream distributions of vorticity concentrations at different $x$-locations show that with actuation, the concentrated shedding of vorticity off the ramp towards the tail boom and the amount of spreading are manipulated such that the vorticity is trapped closer to the surface of the model (Figures 7b). There is a short distance over the ramp subject to a favourable pressure gradient caused by the ramp curvature. The little or no change in the pressure distribution for the baseline flow for $0.08 < x/R < 0.3$ shows the streamwise extent of the recirculation bubble (Figure 6). The significant increase in the suction peak over the ramp from actuation is responsible for the measured deficit in the lift force. This is caused by the larger favorable pressure gradient induced by the increased local velocity of the attached flow. The rapid pressure recovery and corresponding adverse pressure gradient from actuation for $0.08 < x/R < 0.4$ is due to the now attached but expanding flow (cross-stream broadening of the $u$ profiles) over the curved surface. This pressure recovery over the ramp results in the measured reduction in drag with actuation, but it is not large enough to compensate for the induced large suction pressures upstream of the ramp to provide lift enhancements. The combined vectoring of the forces induced by the attachment results in increased pitch-up moment as measured.

The computed streamwise evolution of the flow rate, $Q(z = 0, x)/Q_o = \int u(z = 0, x)\mathrm{d}y/(U_\infty R)$, for the baseline flow field in Figure 8a shows that $Q/Q_o$ is approximately invariant for $0.1 < x/R < 0.30$ (this approximately corresponds to the streamwise extent of the recirculation bubble in Figure 6). It is important to note that $v(0.1 < x/R < 0.40) < 0$ in the centerline plane (see Figure 7d) at the uppermost horizontal boundary of the PIV image. As expected, this suggests that there is net mass flow out of the centerline plane ($0.1 < x/R < 0.30$) as some of the flow over the ramp is pushed outwards symmetrically (+/- $z$-directions) due to the 3-D geometry of the transition section and the presence of the separation bubble. The presence of the tail boom results in the increased flow rate downstream from $x/R = 0.30$. With actuation, the flow rate is greater and increases downstream for $0.1 < x/R < 0.40$ as freestream fluid from above is entrained into the recirculation region. From the mass balance (not shown here), it is noteworthy that there is now net mass flow into the centerline plane from the +/– $z$-directions, most likely from fluid entrained from the sides of the transition section. The integrated $x$-momentum flux at the different streamwise locations given by $P_x(z = 0, x)/P_{x,o} = \int[u(z = 0, x)]^2\mathrm{d}y/(U^2_\infty R)$ are shown in Figure 8b. The higher momentum time-averaged fluid, entrained by the repetitive pulsed actuation, from the

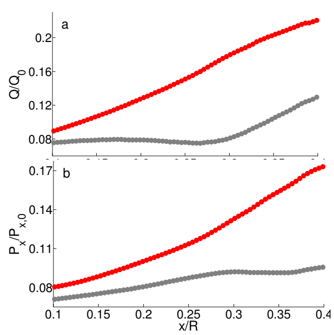


***Figure 8*** *Streamwise evolution of the normalized flow rate, $Q(x)/Q_o$ (a), and integrated x-momentum, $P_x(x)/P_{x,o}$ (b) in the centreline plane, $z = 0$ for the baseline (•) and actuated (•) flows.*

freestream above and from the sides into the lower momentum recirculation region over the transition secton results in overall higher positive $x$-momentum flow than the baseline and hence a reduction in the drag force by ~12%.

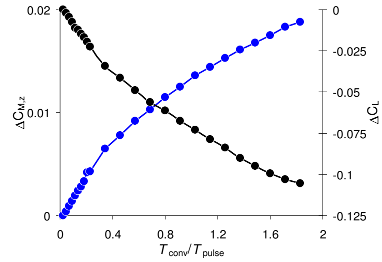


***Figure 9*** *Time-averaged lift force, $\Delta C_L$ (•), and moment about the z-axis, $C_{M,z}$ (•) in the presence of repetitive pulsed actuation at $Re_L = 570{,}000$.*

The effects of the repetition rate, $T_{\text{pulse}}$, are shown in Figure 9 with the time-averaged lift force ($C_L$) and moment about the $z$-axis i.e. pitching moment, ($C_{M,z}$). The monotonic change in $C_L$ and $C_{M,z}$ relative to baseline with decreased time between successive pulses ($T_{\text{pulse}}$) and the asymptotic approach to constant values for $T_{\text{conv}}/T_{\text{pulse}} > 1.4$ highlight the cumulative effects of pulsed actuation, and the disparity in the associated characteristic attachment and relaxation time scales following each pulse as will be shown below. Note that in connection to Figure 9, the time-averaged drag follow a similar asymptotic trend (not shown) where a maximum time-averaged reduction drag of $-\Delta C_D/C_{D,0} \approx 18 - 19\%$ is achieved for $T_{\text{conv}}/T_{\text{pulse}} > 1.4$ (*cf.* $-\Delta C_D/C_{D,0} \approx 12 - 17\%$ for $T_{\text{conv}}/T_{\text{pulse}} = 1.15$).

It is particularly important and informative to investigate the dynamics of the flow over the transition section in further detail. The flow attachment mechanism associated with the response to the pulsed actuation is shown in a sequence of PIV images that are taken phase-locked to the actuation waveform during the repetition cycle of the actuation. Figure 10 shows the phase-averaged flow field obtained

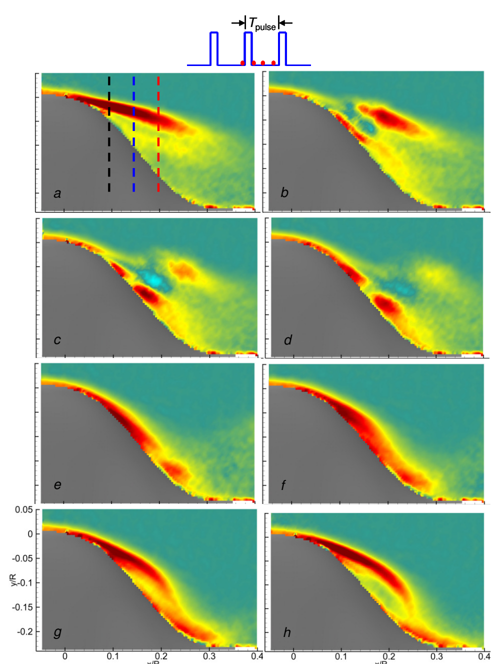


***Figure 10*** *Phase-averaged vorticity concentrations over the transition section between two actuation pulses at $T_{pulse} = 0.87T_{conv}$ apart. The timing of the images is measured relative to the onset of the first pulsed actuation ($t = 0$) at $t/T_{conv}$ = 0.17(a), 0.22 (b), 0.26 (c), 0.30 (d), 0.39 (e), 0.44 (f), 0.52 (g), and 0.70 (h). $\omega L/U_\infty$: -60 60*

from PIV measurements in the $x$-$y$ plane located at the centerline of the model ($z/R = 0$) at different times between successive pulses that are triggered at $T_{pulse}/T_{conv} = 0.87$ apart. A schematic of the PIV images relative to the actuation pulses is included in Figure 10. After the actuation pulse is triggered, the separating shear layer is severed at $t/T_{conv} = 0.17$ (Figure 10a), and by $t/T_{conv} = 0.22$ (Figure 10b), the severed layer forms two distinct structures: a rolled-up CW vortex that is detached from the surface and an attached boundary layer underneath it. The rolled-up severed CW vortex is advected off the surface towards the tail boom while the attached boundary layer continues to grow as it is advected along the surface. As the rolled-up vortex is transported by the cross flow past the end of the transition section, a new separating shear layer is evident. The pulsed severing also results in a distinct CW vorticity concentration that is migrated along the surface ahead of the attached boundary layer (e.g., Figure 10d). From $t/T_{conv} = 0.30$ to 0.44 (Figures 10e-f), the newly-formed boundary layer is advected towards and merges with this downstream vortex, which appears to slow down as a result of the blockage by the tail boom. It is noteworthy that the flow over the transition section is attached from $t/T_{conv} = 0.30$ to 0.44. By $t/T_{conv} = 0.48$ (not shown), the attached flow over the surface begins to relax and the fully attached boundary layer begins to become thicker and peels off the curved surface. This relaxation process continues (Figures 10g-h), and by $t/T_{conv} = 0.61$, the flow is similar to its state before the onset of the actuation pulse (at $t/T_{conv} = 0$). The next actuation pulse follows at $t/T_{conv} = 0.87$ (not shown).

In connection to Figure 10, the formation of vortices by the pulsed actuation leading to the severing of the separating shear layer suggests that characterization of the vorticity flux during the attachment and relaxation between successive pulses is important. The normalized phase-averaged (integrated) vorticity flux, $\Omega/\Omega_0$, in the centerline plane above the transition section between successive pulses with $T_{pulse}/T_{conv} = 0.87$ is shown in Figure 11 where $\Omega(z = 0, x = 0.2R, t) = \int(u.\omega)dy$. At $x/R = 0.2$ downstream of the actuator orifice, the integrated vorticity flux at $t/T_{conv} = 0.17$ begins to decrease relative to the baseline value as actuation is triggered. The integrated vorticity flux is significantly altered by the passing of the actuation vortex pair as indicated by the immediate decrease in the integrated vorticity flux as the vortex is advected past the measurement station. Immediately following this vortex, the vorticity flux is modulated such that a significant amount of CW vorticity is trapped in the attaching boundary layer over the transition section. The streamwise advection speed of the actuation CW vortex is computed from the PIV phases to be $u_{adv}/U_\infty \approx 0.75$ as it is advected through the slow recirculation region above the transition section in close proximity to the faster free stream. Following the attachment process from the actuation pulse, the flow relaxes and is indicated by the slower decrease in the integrated vorticity flux. It is important to note that although the flow is quasi-steady with repetitive actuation, it is clear that there exist transient flow responses between each successive pulse. The rate of attachment, as indicated by the negative slope in the vorticity flux between $t/T_{conv} = 0.22$ and 0.35, is much faster than that of the relaxation process, as indicated by the positive slope in Figure 11 between $t/T_{conv} = 0.4$ and 0.6 (the corresponding normalized rates are –2.5 and 0.9, respectively). Soon after the relaxation process, the flow can be seen to reach steady-state for $t/T_{conv} > 0.57$ before the next pulse is triggered (this is also shown by the approximately zero time-rate of change in the integrated vorticity flux). The trend at other streamwise locations downstream of the actuator orifice are similar to the described trend at $x/R = 0.2$ albeit lower overall magnitudes with increase $x$ as indicative of diffusion in the streamwise direction (see Woo et al., 2011).

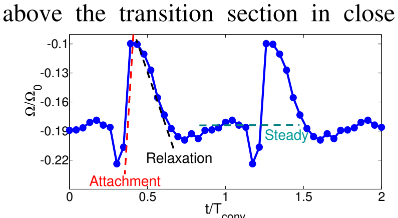


***Figure 11*** *Integrated vorticity flux $\Omega(z, x, t) = \int(u.\omega)dy$ over the transition section within successive pulse actuation at $T_{pulse}/T_{conv} = 0.87$ apart in the x-y plane at $z/R = 0$ and $x/R = 0.2$.*

Details of the transitory 3-D effects of the repetitive actuation are shown using phase-averaged PIV in three, evenly-spaced cross stream ($z$) planes in Figure 12 in the presence of successive actuation. The transient flow separation in the baseline flow appears to be strongly affected by the presence of the tail boom. In the outer cross stream planes at $t/T_{conv} = 0$ just prior to each successive pulse, the separation point is farther downstream (Figures 12a, e and i). A short time after the onset of actuation ($t/T_{conv} = 0.3$), the phase-averaged flow is considerably altered in each plane, but there are noticeable differences in the severed shear layer at the different spanwise locations (Figures 12b, f and j). The subsequent shedding of the CW vorticity concentrations over the ramp is highly 3-D as highlighted in Figures 12c, g and k where the concentrations are closer to the ramp surface for increasing $z$. At $t/T_{conv} = 0.57$, the flow is relaxing in all planes (Figures 12d, h and l) but the attached flow at $z/R = 0.019$ is rapidly peeling off the curved surface while the flow fields at $z/R = 0.038$ and 0.056 are slowly returning to the flow conditions shown in Figures 12e and i, respectively. This suggests that the characteristic attachment and relaxation time scales vary with span.

To quantify the 3-D attachment and relaxation processes of the flow following actuation over the transition section, the phase-averaged integrated vorticity flux at $x/R = 0.2$ are

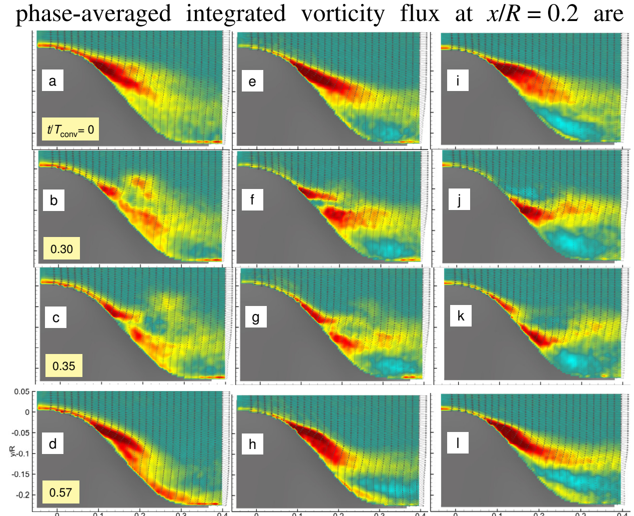


***Figure 12*** *Phase-averaged vorticity contours and velocity vectors of the flow over the transition section in the presence of successive actuation ($T_{pulse}/T_{conv} = 0.87$) at $z/R = 0.019$ (a-d), 0.038 (e-h) and 0.056 (i-l). $\omega L/U_\infty$: -60 60*

plotted in Figure 13 for the two off-center $x$-$y$ planes ($z/R = 0.019$ and 0.038) for comparison with the center plane. The corresponding center plane time-history of the vorticity flux is included in red. It is noteworthy that the flow dynamics following the actuation pulse in the off-center planes are different. In particular, the amplitudes of the changes measured are somewhat smaller for increasing $z$ and hence the time rate of change is smaller between the successive pulses. This suggests that the fastest and largest changes in the flow field in response to pulsed actuation, and the subsequent relaxation are in the centerline plane and hence contribute significantly to the changes in the aerodynamic performance.

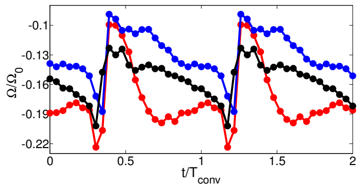

***Figure 13*** *Integrated vorticity flux $\Omega(z, x, t) = \int(u.\omega)dy$ over the transition section following a pulse at $t = 0$ within successive pulse actuation at $T_{pulse}/T_{conv} = 0.87$ apart in the x-y planes at $z/R = 0$ (•), 0.019 (•), and 0.038 (•).*

Recall that symmetric actuation is effected thus far by simultaneous triggering of the two actuator arrays. Figure 14 shows the time-averaged surface pressure distribution over the transition section when only one actuator array is triggered to effect asymmetric repetitive actuation ($T_{pulse}/T_{conv} = 0.87$). At the centerline, the amount of time-averaged pressure recovery is reduced when only one actuator array is triggered suggesting that the extent of flow attachment is smaller (Figure 14a) compared to symmetric actuation. This is in agreement to the measured drag reduction of $-\Delta C_D/C_{D,0} \approx 8 - 9\%$ (*cf.* $-\Delta C_D/C_{D,0} \approx 12 - 17\%$ for symmetric actuation). In addition to the reduced extent of attachment, the off-center pressure distributions in Figure 14b highlight the asymmetric (3-D) pressure recovery (attachmet) resulted from the asymmetric actuation (blue symbols) compared to symmetric actuation (red closed symbol). Of particular importance is that there exists significant spill-over of attached flow over most of the transition section from actuation on one half of the transition section only albeit smaller effects on the unactuated half.

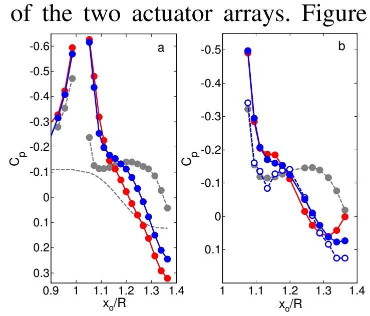

***Figure 14*** *Static surface pressure distributions at centerline ports $z/R = 0$ (a), and offset pressure ports at 35° (b) for the baseline (•), symmetric actuated (•), and asymmetric actuated (•,o) flows. Closed and open blue symbols correspond to the transition section half with and without actuation, respectively.*

It is noteworthy that with asymmetric repetitive actuation, large time-averaged side forces, and both yaw and roll moments are induced by the asymmetric attachment of the flow over the 3-D geometry of the transition section. Figure 15 shows increasing amplitude of the time-averaged increments in side force $\Delta C_S$ and in yaw moment $\Delta C_{M,y}$ with decreasing time between successive pulses. In connection to the lift and drag forces, and the pitching moment in Figure 9, an asymptotic time-averaged value for the side force, yaw and roll (not shown) moments is reached with repetitive actuation. For $T_{pulse}/T_{conv} = 0.87$, the time-averaged side force induced by only one actuator array being triggered is $\Delta C_S/C_{D,0} = +/-13\%$ which could be exploited to improve the maneuverability of the airframe.

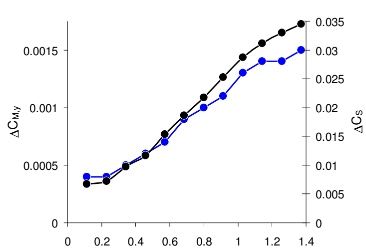

***Figure 15*** *Time-averaged side force, $\Delta C_S$ (•), and yaw moment, $C_{M,y}$ (•) in the presence of repetitive pulsed actuation at $Re_L = 570{,}000$.*

## V. TRANSITORY ENHANCEMENT OF AERODYNAMIC FORCES AND MOMENTS

As demonstrated above, the effects of actuation can be tailored to bias the time-averaged aerodynamic forces and moments using actuation schemes that promote assymetric attachment over the transition section. Woo et al. (2011) also demonstrated that with the use of a burst of pulses the aerodynamic forces can be modulated. In this section, the transients associated with the onset and termination of a burst of pulses are investigated using symmetric and asymmetric actuation to further exploit the control authority of the low-duty cycle burst-modulated actuation. Figure 16 shows the schematic timing sequence when using "bursts" of multiple pulses each that are repeated at low actuation duty cycle where the three actuation parameters, $N$, $T_{pulse}$, and $T_{delay}$ (between bursts), are varied independently. The six-element actuator array is divided into two adjacent spanwise segments that can be triggered simultaneously in or out of phase.

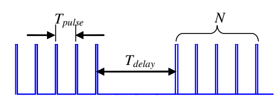


***Figure 16*** *Schematic timing sequence for "bursts" of multiple pulses.*

In connection to Figure 9 above, the time-averaged aerodynamic forces (drag and lift) and moment (pitch-axis) effected by the symmetric repetitive actuation reaches an asymptotic level with increasing repetition rate (decreasing $T_{pulse}$). It is with this in mind that the transitory effects associated with the onset and termination of actuation for different $T_{pulse}$ are investigated here. The response of the flow over the model is assessed from measurements of the global aerodynamic forces and moments that are sampled phase-locked to the actuation waveform. Figures 17a and b show the phase-averaged lift force and the pitching moment (taken about $x_o/R = 0.34$) relative to baseline, respectively, over two burst periods. Actuation is triggered at $t = 0$, and a constant burst and delay period of $T_{burst}/T_{conv} = T_{delay}/T_{conv} = 22$ is used while $T_{pulse}/T_{conv}$ is increased from 0.76 to 9.1. It is interesting that the build-up of the forces and moments at the onset of actuation is highly

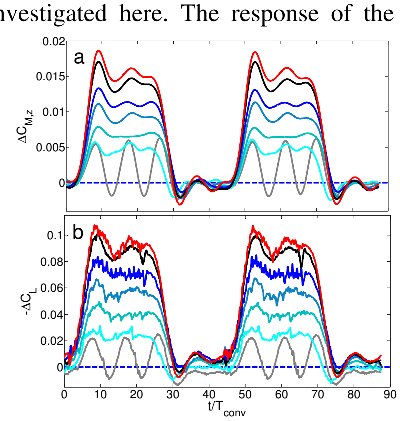

***Figure 17*** *Transitory manipulation of aerodynamic pitching moment $\Delta C_{M,z}$ (a) and lift force $-\Delta C_L$ (b) using a burst of pulses $T_{burst}/T_{conv} = T_{delay}/T_{conv} = 22$ for $T_{pulse}/T_{conv} = 0.76$ (•), 0.87 (•), 1.14 (•), 1.82 (•), 3.0 (•), 4.55 (•) and 9.1 (•). Both bottom actuator arrays are triggered in phase with each other.*

sensitive to $T_{pulse}$. Within 8-10$T_{conv}$ the maximum change in the pitching moment and lift force is measured for the different $T_{pulse}$ which highlights the rapid flow response to actuation. However, the maximum measured value is smaller for longer $T_{pulse}$ due to the increasing time for the flow to relax between each pulse and this maximum is detected slightly earlier with decreasing $T_{pulse}$. For example, $|\Delta C_L|_{max} = 0.107$ is measured at $t/T_{conv} = 8.4$ for $T_{pulse}/T_{conv} = 0.76$, and $|\Delta C_L|_{max} = 0.049$ is measured at $t/T_{conv} = 9.7$ for $T_{pulse}/T_{conv} = 3.0$. The transitory flow attachment as indicated by the reduction in lift force is accompanied by rapid reduction in drag following the onset of actuation (not shown). Within the first five pulses for $T_{pulse} = 0.87T_{conv}$, the drag decreases by $-\Delta C_D/C_{D,0} \approx 18\%$ (*cf.* the time-averaged reduction as a result of repetitive actuation is $-\Delta C_D/C_{D,0} \approx 12\%$). The rates at which the forces and moments are changing at the onset of actuation are also increasing as the repetition rate is increased. Following the termination of the burst as the suction on the surface downstream of the actuators decreases, the flow begins its periodic separation before the onset of the next burst where the global rate at which the flow relaxes to baseline is similar to that of the corresponding attachment. Perhaps more important is that when $T_{pulse}$ is longer than a threshold value that is commensurate with the global relaxation time scale the flow relaxes completely to its baseline as is evident by the large oscillations in the measured force and pitching moment for the case where $T_{pulse}/T_{conv} = 8.7$ (Figures 17 and 19). It is also noteworthy that for $T_{pulse}/T_{conv} = 4.55$ the number of pulses that is required to reach the steady-state value is only about $N = 3$.

In Figure 18, the number of pulses is increased while maintaining $T_{pulse}/T_{conv} = 0.87$ with synchronous triggering of the two actuator arrays. The pitching moment and the lift force increments relative to baseline, phase-averaged over two burst periods, are shown in Figures 18a and b, respectively. It is important to note that the number of pulses required to reach the steady-state values which is indicative of attachment, is approximately ten. Any additional pulses triggered at $T_{pulse}/T_{conv} = 0.87$ simply maintains the time-averaged aerodynamic forces at the steady-state value. In connection to Figures 21 - 22 below, the significant increase in aerodynamic forces and moments in Figure 18 for the case with only $N = 5$ suggests that the flow has almost reached quasi-steady attachment within that short time. The global forces and moments on the model have almost reached quasi-steady values (albeit somewhat smaller than the peak values that require $N \geq 10$) before the termination of the actuation allows the flow to return to baseline. This has demonstrated that burst actuation can be exploited for cyclic control of the flow to achieve large forces and moments on the model in a short response time. This may be useful during forward flight of a helicopter which experiences periodic aerodynamic loads such as those induced by the rotor.

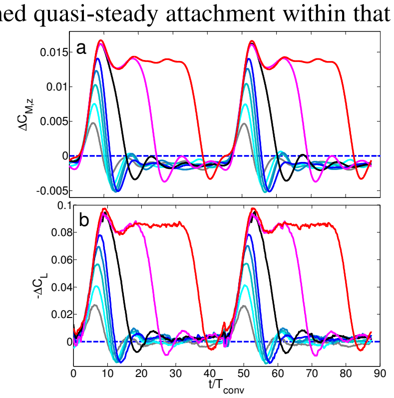


***Figure 18*** *Transitory manipulation of aerodynamic pitching moment $\Delta C_{M,z}$ (a) and lift force $-\Delta C_L$ (b) using a burst of pulses $T_{pulse}/T_{conv}$ = 0.87 for N = 1(●), 2 (●), 3 (●), 4 (●), 5 (●), 10 (●), 20 (●), and 35 (●). Both bottom actuator arrays are triggered in phase with each other.*

The transitory control authority of burst-modulated actuation suggests that it can be effective for manipulating the aerodynamic forces on the airframe on time scales that are commensurate with airframe maneuvers without the presence of mechanical control surfaces. Of particular interest is manipulation of the side forces on the airframe. This is accomplished using asymmetric actuation that is effected by driving the two actuator segments within the row out of phase with each other (i.e., at any given instant control is effected with one three-element array) to improve yaw maneuverability (Figure 19). The aerodynamic forces and moments relative to baseline are phase-averaged over two burst periods. Upon actuation, the model experiences a rapid change in the side force and simultaneous drag reduction (albeit smaller amplitude *cf.* to symmetric actuation) that is induced by the attachment of the separated flow over the corresponding spanwise half of the transition section. As shown in Figure 19a, the maximum measured changes in $C_S$ increase for shorter $T_{pulse}$ as expected from the monotonic increase in the time-averaged $C_S$ with repetition rate (Figure 15). The smaller degree of attachment achieved using asymmetric actuation result in smaller transitory changes in the lift force and pitching moment (*cf.* Figure 17 and 18). It is also interesting to note that transients in $C_L$, $C_{M,z}$ and $C_D$ (not shown) during asynchronous burst-actuation are greatly reduced due to the fact that these transients as induced by the onset and termination of one actuator array are offset by the transients of the other out-of-phase actuator array (Figures 19b and c). The yaw moment in Figure 19d and roll moment (not shown) show similar trend to the side force transients as evidence to the control authority of using asymmetric actuation where improved aerodynamic performance of the airframe is achieved.

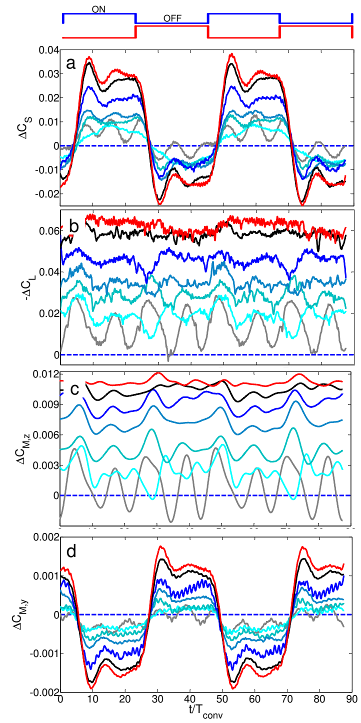


***Figure 19*** *Transitory manipulation of aerodynamic side force $\Delta C_S$ (a), lift force $-\Delta C_L$ (b), pitching moment $\Delta C_{M,z}$ (c), and yaw moment $\Delta C_{M,y}$ (d) using a burst of pulses $T_{burst}/T_{conv}$ = $T_{delay}/T_{conv}$ = 22 for $T_{pulse}/T_{conv}$ = 0.76 (●), 0.87 (●), 1.14 (●), 1.82 (●), 3.0 (●), 4.55 (●) and 9.1 (●). The bottom actuator arrays are triggered 180° out of phase with each other (schematic of the actuation signals are included at top).*

Figure 20 demonstrates that the control authority of the pulsed actuation in manipulating the forces and moments on the model can be exploited in an additive manner. Figures 20b-d show the aerodynamic performance (phase-averaged over two burst periods) for the different actuation configurations shown in Figure 20a. Actuation schemes (i) and (ii) are already demonstrated in Figures 17 – 18 above, but are included here for reference. Actuation schemes (iii) and (iv) utilize burst-modulated actuation using only one actuator array. It is noteworthy that due to the spill-over effect of the actuation (i.e. asymmetric attachment) the changes in the lift and pitching moment relative to baseline reach approximately 75% of the quasi-steady values when both actuators are triggered together (Figures 20b and d). On the other hand, these two actuation schemes result in transitory changes to the side force (Figure 20c) that are attributed to only the corresponding half of the total change in $C_S$ when both actuators are triggered out of phase (*cf.* Figure 19). This suggests that the spill-over effect when combined with the symmetric 3-D geometry of the transition section contributes significantly and positively to $C_{M,z}$, $C_D$ and $C_L$ but can contribute negatively (albeit in only a very small extent) to $C_{M,x}$, $C_{M,y}$ and $C_s$. Actuation schemes (v) and (vi) demonstrate that the control authority of the pulsed actuation can be utilized in an additive manner by burst-triggering one of the actuator arrays in the presence of repetitive actuation from the other actuator array which establishes a new baseline.

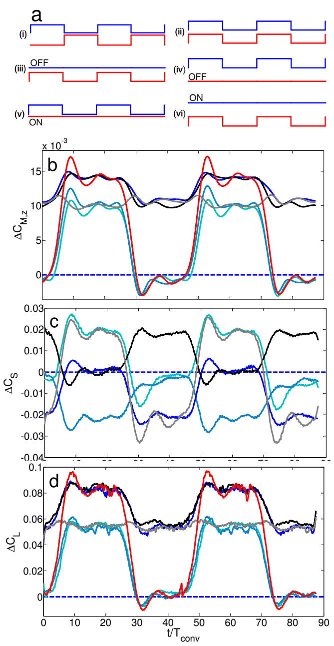


***Figure 20*** *Transitory manipulation, using different symmetric and asymmetric actuation schemes (a), of the aerodynamic pitching moment $C_{M,z}$ (b), side $C_S$ (c), and lift $C_L$ (d) forces, using a burst of pulses at $T_{pulse}/T_{conv} = 0.87$ with $T_{burst}/T_{conv} = T_{delay}/T_{conv} = 22$ (i.e. $N = 25$). The line traces corresponding to the actuation schemes are – (i), – (ii), – (iii), – (iv), – (v), and – (vi).*

It is important to understand the mechanism by which the side force is created. Figure 20c shows the side force created by each actuator array individually using burst of 25 pulses (actuation scheme (i)). It is evident that the extent of flow attachment achieved with each actuator array is similar (albeit small difference in the change in side force due to a slight difference in actuator performance). Although there is a small spill-over effect in attaching the flow when the actuator arrays are operated individually, the combined effect of the actuators when operated together but out of phase with each other highlights that the individual effects are additive. Perhaps more important is that the time scales associated with the combined actuation scheme are much shorter as evident in the short response time needed for the model to experience the switching of the actuator arrays.

As demonstrated above by the high authority of the actuation pulse in attaching the separated flow over the transition section, the highly transitory response of the flow to each pulse is investigated using load cell and PIV measurements to determine the transient flow dynamics associated with the onset and termination of actuation. As discussed above in connection to Figure 18, using a burst of $N = 5$ pulses triggered at $0.87T_{\rm conv}$ is sufficient for investigating the associated transients as the extent of attachment achieved is close to that of the saturation level (see Figures 9 and 15 for the time-averaged levels).

Figure 21 shows the phase-averaged flow fields for the two cases of actuation where a burst of five pulses ($N = 5$) with $T_{\rm delay}/T_{\rm conv} = 15.2$ from the two actuator arrays are triggered simultaneously (Figures 21 a-h) and out-of-phase (Figures 21 i-p). For the synchronous (asynchronous) actuation, both actuator arrays (first actuator array) are triggered at $t = 0$. The last (5th) pulse for synchronous actuation is triggered at $t/T_{\rm conv} = 3.5$. For the asynchronous actuation, the last (5th) pulse from one actuator array is triggered at $t/T_{\rm conv} = 3.5$ while the second array is first triggered at $t/T_{\rm conv} = 3.7$ and its last (5th) pulse is triggered at $t/T_{\rm conv} = 7.2$. In connection to Figure 22, the slight overlap in timing of actuation pulses between the two actuator arrays when triggered asynchronously results in significantly larger changes to the flow field than that induced by only one actuator array. It is noteworthy that the differences in the centerline plane ($z = 0$) flow fields between the two cases are significant and

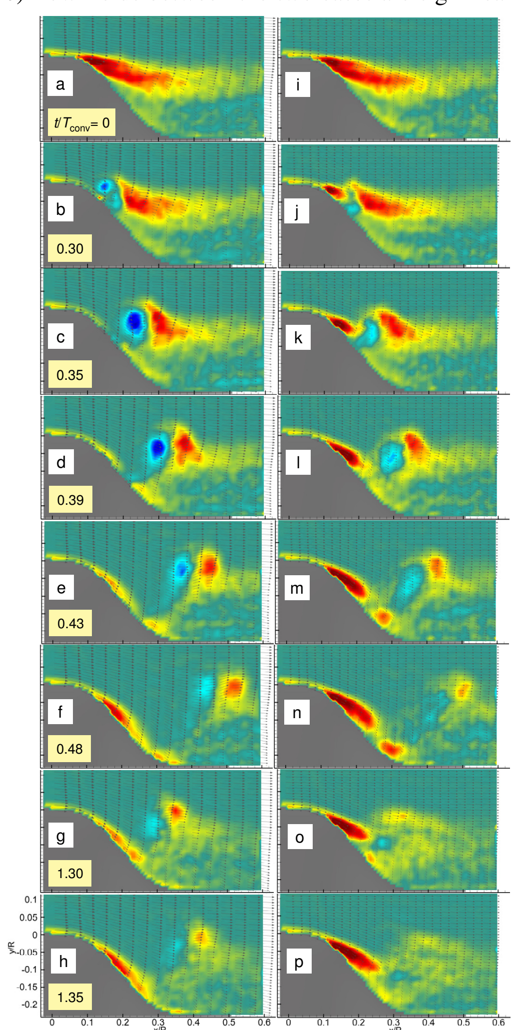


***Figure 21*** *Phase-averaged vorticity contours and velocity vectors of the flow over the transition section in the presence of successive 5-pulse actuation ($T_{pulse}/T_{conv} = 0.87$) at $z/R = 0$. Actuation from the two actuator arrays are triggered simultaneously (a-h) and out of phase (i-p). $\omega L/U_\infty$: -60 ▬ 60*

contribute to the majority of the differences in the transients observed in the global attachment and relaxation processes. This can be explained, in connection to Figures 12 and 13, due to the largest increments in the magnitude and time rates of change in the flow at the centerline plane following the onset of the burst actuation compared to the corresponding smaller and slower changes in the flow measured in the off-center planes.

The flow above the transition section at $t/T_{\mathrm{conv}} = 0$ for the two actuation cases (Figures 21a and i) are identical as the flow is allowed to relax completely to baseline. At $t/T_{\mathrm{conv}} = 0.3$, the separated shear layer is severed by the first actuation pulse from both arrays (Figure 21b) and from only one of the actuator segments (Figure 21j). It is evident that the pulse strength as provided by the actuators triggered simultaneously is stronger than that of only one of the actuator segments. The subsequent flow transients following the first pulse at $t/T_{\mathrm{conv}} = 0.35$ and 0.39 highlight the significantly better attached flow over the transition section and a much thinner attached boundary layer for the simultaneously triggered actuation (Figures 21c – d) than the asynchronous actuation (Figure 21k – l). The higher concentrations of vorticity associated with the severing and shedding of the shear layer and the continued growth of the much thinner attached boundary layer for symmetric actuation even at $t/T_{\mathrm{conv}} = 0.43$ and 0.48 (Figures 21e– f) suggests better attachment (*cf* Figures 21m – n for asynchronous actuation) which is in agreement with the larger changes in the transitory aerodynamic forces and moments on the airframe (Woo et al. 2011). In a similar manner, there are differences in the relaxation process following the first pulse and before the onset of the second pulse between the two actuation schemes. It is evident at $t/T_{\mathrm{conv}} = 0.48$ that the peeling off of the attached boundary layer occurs more rapidly for the out-of-phase (Figure 21n) than the synchronous (Figure 21f) actuation scheme. Perhaps more important is that the flow field following the onset of the second pulse, from either actuation scheme, is significantly different from that following the first pulse. The reduced strength in the shed vortices and the downstream extension of the attached boundary layer over the curved surface at $t/T_{\mathrm{conv}} = 1.3$ and 1.35 (Figures 21g – h and o – p) show, in connection to Figure 22, reduced actuation effects as the flow field is already better attached following the first pulse. The flow fields following subsequent pulses are reasonably similar suggesting that the actuation transients approach quasi-steady conditions.

Woo et al. (2011) showed that the flow rate at a location closer to the orifice experiences a faster relaxation process than at a location closer to the tail boom for the two actuation schemes. This is also the case in the integrated vorticity flux where it is evident that the rate of vorticity shedding during the relaxation process is higher than at the location closer to the tail boom. Figure 22 compares the flow rate and the integrated vorticity flux, in the center plane, at the streamwise location $x = 0.2R$ downstream of the actuator orifice for the two 5-pulse actuation schemes above. In connection to the phase-averaged load cell measurements (not shown) and the PIV images in Figure 21, the two actuation schemes show similar qualitative flow behaviors but the details of the computed quantities highlight larger changes in the flow field with simultaneous actuation as evident by the larger extent of attachment achieved with this symmetric actuation scheme. This is in agreement with the consistently larger flow rate and vorticity flux from symmetric actuation (Figures 22a and b, respectively) which indicate higher entrainment of the free stream fluid and more effective severing of the separating shear layer. It is clear that the most significant attachment effect is from the first pulse for both actuation schemes as evident from the largest changes in the integrated vorticity flux following the first pulse (Figure 22b). The effects of subsequent pulses are somewhat diminished due to the reduced extent of the separated flow following the first pulse. It is important to note that the attachment effects for all the pulses are somewhat smaller for the out-of-phase actuation scheme than the synchronous actuation. This results in the smaller changes in measured flow rate and integrated vorticity flux for $t/T_{\mathrm{conv}} < 3.5$ and $t/T_{\mathrm{conv}} > 5$ when actuation is provided with only one actuator array. It is noteworthy that although the global effects are smaller for the out-of-phase burst actuation as indicated by the changes in the flow rate and integrated vorticity flux, the manipulation of the vorticity concentrations in the separated shear layer using the two actuator arrays triggered out of phase and its spill-over effects can induce large transitory side forces, roll and yaw moments due to the asymmetric actuation without significant reduction in effectiveness to reduce drag and pitching moment control.

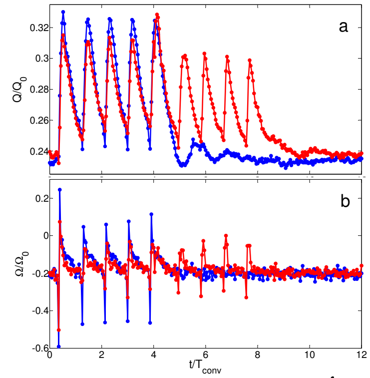


***Figure 22*** *Flow rate $Q(z, x, t) = \int u dy$ (a) and integrated vorticity flux $\Omega(z, x, t) = \int (u.\omega) dy$ (b) in the centerplane $z = 0$ over the transition section following a 5-pulse triggered simultaneously (•) and out of phase (•) with $T_{pulse}/T_{conv} = 0.87$ apart. The streamwise location is $x/R = 0.2$ downstream of the actuator orifice.*

## VI. CONCLUSIONS

The effectiveness of pulsed actuation for controlling the separation on the transition section to the tail boom of a ROBIN mod7 rotorcraft fuselage is investigated in wind tunnel experiments. The actuation is effected by an azimuthally-segmented array of momentary, combustion-based actuator jets having a characteristic time scale O[1 ms] that is an order of magnitude shorter than the convective time scale of the flow. The actuators are placed upstream of the model's transition region, and their interactions with the massively separated cross flow in this domain and effects on the global aerodynamic forces and moments are assessed from load cell measurements and high resolution PIV.

The three-dimensional separation of the baseline flow is characterized using pressure and PIV measurements. The separation on the transition section is preceded by a large suction peak that is followed by a slow pressure recovery towards the tail boom. It is shown that within the range of the present experiments, the separation line that extends along the sides of the model is insensitive to the model's angle of attack and free stream speed. While the extent of the separation domain decreases with increased nose-down pitch of the model, the drag increases as a result of contributions by the front end of the model and the tail boom. It is noteworthy that the presence of the boom affects the degree of separation in the center plane, and the attachment is more pronounced closer to its spanwise edge.

The effects of repetitive pulsed actuation are investigated when the entire azimuthal array is triggered simultaneously ($\alpha = 0°$, Re = 570,000). In the absence of actuation, separation is severe and occupies the majority of the fuselage's transition section. The baseline flow is highly three-dimensional with significant spanwise flow away from the centerline plane where separation is strongest. Closer to the spanwise edge of the transition section the baseline flow separates farther downstream and the extent of spanwise flow is reduced. When actuation is applied and the time between successive pulses of the actuation pulse train is reduced, the domain of attached flow is extended with significant changes in the time-averaged aerodynamic lift and drag forces, and the pitching moment. The cumulative effect of repetitive actuation ultimately reaches an asymptotic level of maximum flow attachment for which a reduction of 12–17% in the total drag is achieved with $T_{\mathrm{pulse}}/T_{\mathrm{conv}} = 0.87$. Measurements of the flow field in the center plane show that the time averaged flow is attached and that the reversed flow over the aft surface is significantly suppressed with a significant volume flow rate of entrained fluid from the freestream above the ramp and sides of the model. The attached flow is associated with a significant increase in the suction pressures on the flat surface of the model and the juncture upstream of the ramp.

Phase-averaged PIV images demonstrate that flow attachment occurs in a cycle that is commensurate with the periodic pulsed actuation which is based on a cyclical onset and suppression of a separation bubble. The actuation leads to severing of the separating shear layer and to the formation of a detached vortex that is advected with the cross flow while the vorticity layer that follows is attached to the surface during a significant segment of the actuation cycle. The relaxation of the attached flow follows as the attached boundary layer peels off the surface. It is determined, from the phase-averaged PIV measurements taken in different spanwise planes, that the flow transients associated with successive pulses are most prominent in the centerline plane where the transitory changes in the flow field are largest, and the attachment and relaxation time scales are the shortest. The flow transients are slower and diminish in magnitude towards the spanwise edge of the transition section where the streamwise extent of the separation bubble on the ramp decreases.

The demonstrated control authority of successive pulsed actuation and the observed disparity in the spanwise flow attachment and relaxation time scales are exploited to induce large transitory forces and moments on the model using burst-modulated actuation. It is shown that with $T_{\mathrm{pulse}}/T_{\mathrm{conv}} = 0.87$ the transitory aerodynamic forces and moments reach their quasi-steady values within ten successive pulses triggered simultaneously. However, the majority of the enhancement in the aerodynamic performance can be achieved with as few as $N = 5$ pulses. By momentarily attaching the flow asymmetrically over nominally half of the transition section large transient changes in side forces ($\Delta C_S/C_{D,0}$ = +/-13%) are induced to enhance roll and yaw maneuverability while still achieving a significant quasi-steady drag reduction. The additive nature of the flow attachment when coupled to the 3-D geometry of the transition section allows for multiple actuation configurations where different aerodynamic performances can be achieved. It is also shown using phase-averaged PIV measurements in the centerline plane and force measurements that the symmetric and asymmetric attachment using only five pulses from each actuator array can generate rapid enhancement of asymmetric aerodynamic forces and moments on the model.

## ACKNOWLEDGMENTS

This project has been supported under a Phase II SBIR program from the U.S. Army monitored by Dr. Preston Martin whose technical guidance and support are gratefully acknowledged.

## REFERENCES

Ahuja, K. K., and Burrin, R. H., "Control of flow separation by sound", AIAA 84-2298.

Brzozowski, D., and Glezer, A., "Transient Separation Control Using Pulse-Combustion Actuation", AIAA Paper, 3rd AIAA Flow Control Conference, 2006-3024, 2006.

Brzozowski, D., Woo., G. T. K., Culp, J., and Glezer, A., "Transient Separation Control using Pulse-Combustion Actuation," *AIAA J*., **48**, 2482-2490, 2010.

Crittenden, T., Glezer, A., Funk, R., and Parekh, D., "Combustion-Driven Jet Actuators for Flow Control," AIAA Paper 2001-2768, 2001.

Crittenden, T., Warta, B., and Glezer, A., "Characterization of Combustion Powered Actuators for Flow Control," AIAA Paper 2006-2864, 2006.

Honohan, A., Amitay, M., and Glezer, A., "Aerodynamic Control using Synthetic Jets," AIAA Paper 00-2401, 2000.

Neuberger, D., and Wygnanski, I., "The Use of a Vibrating Ribbon to Delay Separation on Two Dimensional Airfoils", Proc. of Air Force Academy Report TR-88-0004, 1987.

Seifert, A., Darabi, A., and Wygnanski, I., "Delay of Airfoil Stall by Periodic Excitation," *Journal of Aircraft*, **33-No.4**, 691-698, 1996.

Sosa, R., Artana, G., Moreau, E., and Touchard, G., "Flow Control With EHD Actuators in Middle Post Stall Regime," *Journal of the Brazilian Society of Mechanical Science and Engineering*, **XXVIII-No.2**, 200-207, 2006.

Tuck, A., and Soria, J., "Active Flow Control over a NACA 0015 Airfoil using a ZNMF Jet,"*15th Australasian Fluid Mechanics Conference*, 2004.

Woo, G. T. K., Crittenden, T., and Glezer, A., "Transitory Control of a Pitching Airfoil using Pulse Combustion Actuation," AIAA Paper 08-4324, 2008.

Woo, G. T. K., Crittenden, T., and Glezer, A., "Transitory Separation Control over a Stalled Airfoil," AIAA Paper 09-4281, 2009.

Woo, G. T. K., and Glezer, A., "Transient Control of Separating Flow over a Dynamically-Pitching Airfoil," AIAA Paper 2010-861, 2010.

Woo, G. T. K., and Glezer, A., "Transitory Control of Dynamic Stall on a Moving Airfoil," AIAA Paper 2011-0489, 2011.

Woo, G. T. K., Glezer, A., Bain, J., Sankar, L., and Crittenden, T., "Rotorcraft Fuselage Drag Reduction using Combustion Powered Actuators," AIAA Paper 2011-34, 2011.